Matching 3D OCT Retina Images into Super-Resolution Dataset

Agnieszka Stankiewicz[1], Tomasz Marciniak[1], Adam Dąbrowski[1]

[1]Division of Signal Processing and Electronic Systems
Chair of Control and Systems Engineering
Faculty of Computing
Poznan University of Technology
Poznan, Poland
tomasz.marciniak@put.poznan.pl

Marcin Stopa[2,3], Elżbieta Marciniak[2], Andrzej Michalski[2]

[2]Clinical Eye Unit and Pediatric Ophthalmology Service,
Heliodor Swiecicki University Hospital,
Poznan University of Medical Sciences
Poznan, Poland
[3]Department of Optometry and Biology of Visual System,
Poznan University of Medical Sciences
Poznan, Poland
stopa@ump.edu.pl

Abstract—**Optical coherence tomography (OCT) is the current very fast and accurate modality for noninvasive assessment of 3D retinal structure. Due to large amount of data acquired with this technique the resolution of 3D scans is limited. In this paper we present a new method for improving resolution of 3D macula scans while maintaining short acquisition time and robustness with respect to motion artifacts. Our approach is based on multi-frame super-resolution method applied to several 3D standard resolution OCT scans. Presented experiments where performed on volumetric data acquired from adult patients with the use of Avanti RTvue device. Each OCT cross-section (B-scan) was subjected to image denoising and retinal layers segmentation. The generated 3D super-resolution scans have significantly improved quality of the vertical cross-sections.**

Keywords – OCT, super-resolution, multi-frame, retina image segmentation

I. INTRODUCTION

Algorithms for biometric analysis of retina images are very valuable to clinicians, as they lead to expansion of diagnostic procedures. Implementation of non-invasive diagnostic methods, such as optical coherence tomography (OCT) in modern visualization systems allows to investigate the causes of ever more frequent lesions in the eye [1].

Proper detection of retinal layers and existing pathologies is critical for diagnosis and further treatment [2]. Factors that significantly impede segmentation process are low quality of acquired images (due to heavily noisy data or uneven tissue reflectivity). Currently used algorithms in spite of high efficiency cannot cope with this type of artifacts.

Volumetric OCT scan consists of a set of measurements called A-scans representing retinal tissue in depth in a single retina point. Any vector of A-scans creates a cross-section (B-scan) in one direction, and a collection of B-scans is referred to as the 3D OCT examination.

Unfortunately, a typical 3D examination obtained with the fast scanner working in the horizontal direction will cause lower data resolution in the vertical direction. It is not possible to retrieve data between the cross-sections even with the use of interpolation algorithms. The calculated information would be inexact and not sufficient for the detailed, three-dimensional analysis of investigated pathologies or vessels modeling.

Innovative approach presented in this article involves combination of multiple 3D scans into one super-resolution scan. The proposed solution addresses this problem by approximating detailed informative content in spaces between subsequent OCT cross-sections. The data obtained from multiple examinations of macular area takes into account displacements between the scans. This will counter for the poor resolution of the retinal thickness maps produced by OCT, which is the biggest disadvantage of OCT and still remains to be solved in forthcoming OCT models [3].

II. SUPERRESOLUTION IN OCT

A. State-of-the-art

Biomedical imaging devices have limited achievable resolution due to both theoretical and practical constraints. Table 1 presents standard resolutions of the 3D OCT examinations for selected devices.

TABLE I. STANDARD RESOLUTIONS OF 3D EXAMINATION FOR TOPCON [4], AVANTI [5] AND COPERNICUS [6] DEVICES

Device	Topcon Triton	Avanti RTvue	Copernicus
Data resolution [px]	256×512×992	141×385×640	100×800×1010
Volume [mm]	6×6×3	7×7×2	8×8×2

Typical 3D OCT scan acquired with the speed of 70 000 A-scans / second with the resolution of 141×385 A-scans takes approximately 0.94 second [5]. Such examination, representing a volume of 7×7×2 mm, has unequal data resolution (141×385×640 pixels, respectively) in respect to the measured tissue. An example of horizontal and vertical cross-section from such scan is illustrated in Fig. 1 (fast scanner working in the horizontal direction). As can be seen, B-scan corresponding to the vertical direction in the eye is deficient (presents discontinuities, and extrapolated data samples).

This work was prepared within the PRELUDIUM CADOCT-Project number 2014/15/N/ST6/00710 founded by National Science Centre Poland.

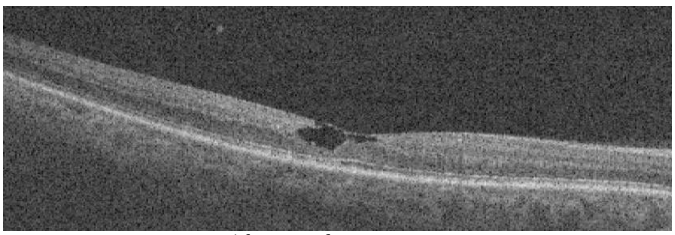

a) horizontal cross-section

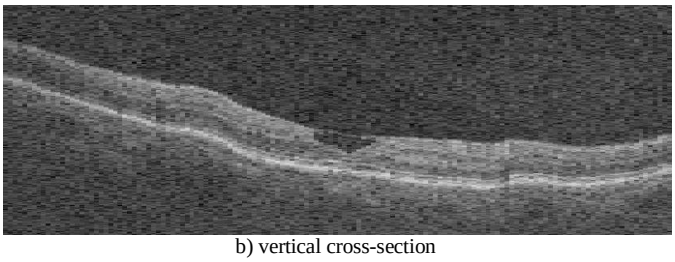

b) vertical cross-section

Figure 1. B-scans of volumetric data in vertical and horizontal directions

It should be noted that data acquisition of an ideal scan with uniform data distribution would take about 2 to 3 times longer examination. This, on the other hand, is unacceptable, since an ill person cannot be handled long in time, due to problems with eye fixation or pain. Additional disadvantage of a single scan is an uneven tissue illumination in peripheral areas.

Fortunately, spatial resolution of acquisition devices can be enhanced by post-processing. A class of techniques dedicated to overcome this limitation is called super-resolution (SR) [7]. Their objective is to produce a high resolution (HR) image from a series of low resolution (LR) ones.

The idea of SR significantly differs from simple interpolation techniques. Methods such as bilinear, or bicubic interpolation introduce no new information into the SR image and generally blur it, while the application of SR attempts to increase informative content of the restored image [8].

The SR techniques can be divided into those relying on a single LR input image (single-frame) or those based on a set of images of the same scene (multi-frame). The advantage of multi-frame SR algorithms is the ability to use the sub-pixel shifts between many LR images. The gathered information is then fused into a HR picture with improved scene description.

This is an attractive feature to exploit for biometrics (i.e. face [9] and iris [10] recognition) and medical purposes, since high resolution images are necessary for visualization and understanding of the examined tissue. For several years now attempts of SR for biomedical applications have been made, manly in:

- X-ray imaging [11], Computed Tomography (CT) [12] and Magnetic Resonance Imaging (MRI) [13][14]
- positron emission tomography (PET) [15]
- ultrasonography (US) [16]
- histology [17][18].

The tomographic images (MRI, CT, and OCT) are usually composed of a set of cross-sections. Thus, the resolution of data is anisotropic and the images have high quality only within the slices [19]. This is why, the super-resolution methods are valuable for examinations obtained with these types of devices.

Numerous SR techniques proposed for the use in medical applications were classified by [8] into two groups: adaptive interpolation and compressed sensing methods. The first class of algorithms attempts to replicate the characteristic structures (such as edges) from LR into SR images. These are the learning methods based on the nearest neighbors interpolation [12][15], neural networks [17], confidence map [19], principal component regression [20]. One of the problems that encounter the example-based algorithms, that try to learn the relationship between the LR and HR images, is the dependence from the database that provides these image patch pairs.

The second group of methods, based on the concept of sparsity, includes total variation regularization [11], and sparse-coding-based SR [21][22]. Their disadvantage is sensitivity to characteristics of the acquisition system.

A very interesting solution presented by [12] and [19] utilized two orthogonal low resolution datasets to compose a single HR image. The conducted tests gave promising results for both CT and MRI modalities.

One of the problems encountered during the acquisition of the OCT data is the inevitable eye movements. Nevertheless, slight discrepancies between any pair of scans in the set (caused by motion) are useful in the case of SR reconstruction. The geometric transformations detected with sub-pixel accuracy provides valuable information. Additionally, it has been proven that combination of multiple volumetric registrations provides slices of higher quality [23].

For the use in OCT imaging the multi-exposure acquisition is performed solely for noise reduction on a singular cross-section trough the center of macula and optic disc [24]. Such averaging technique is not feasible for 3D retina reconstruction due to long scanning time.

B. Algorithm

In this section we propose a method for improving the density of gathered 3D data in OCT images. The general idea of maximizing informative content of volumetric retina representation comes from the problem of uneven data distribution. The algorithm will be presented on data gathered with the use of Avati RTvue device, but is applicable to any other OCT imaging devices.

Data cube for the selected device represents 141×385×640 measurement points corresponding to the tissue volume of 7×7×2 mm as was mentioned in Table 1. This means that the information about the retina structure between the adjacent slices is virtually unknown, and may have terrible consequences in the pathology detection.

The proposed algorithm for super-resolution dataset with detailed volumetric representation of the retina structure consists of the following steps:

1) Acquisition and prepocessing of images

To construct a HR volumetric scan, we use a set of sequentially recorded low-resolution 3D scans. Each 3D scan is centered at the macula and consists of a raster of B-scans. The number of 3D scans to be used is unlimited, although at least two are necessary. The first step includes also noise reduction by application of anisotropic diffusion filter, as was proven to be a good choice for both pathologic and healthy eyes [25].

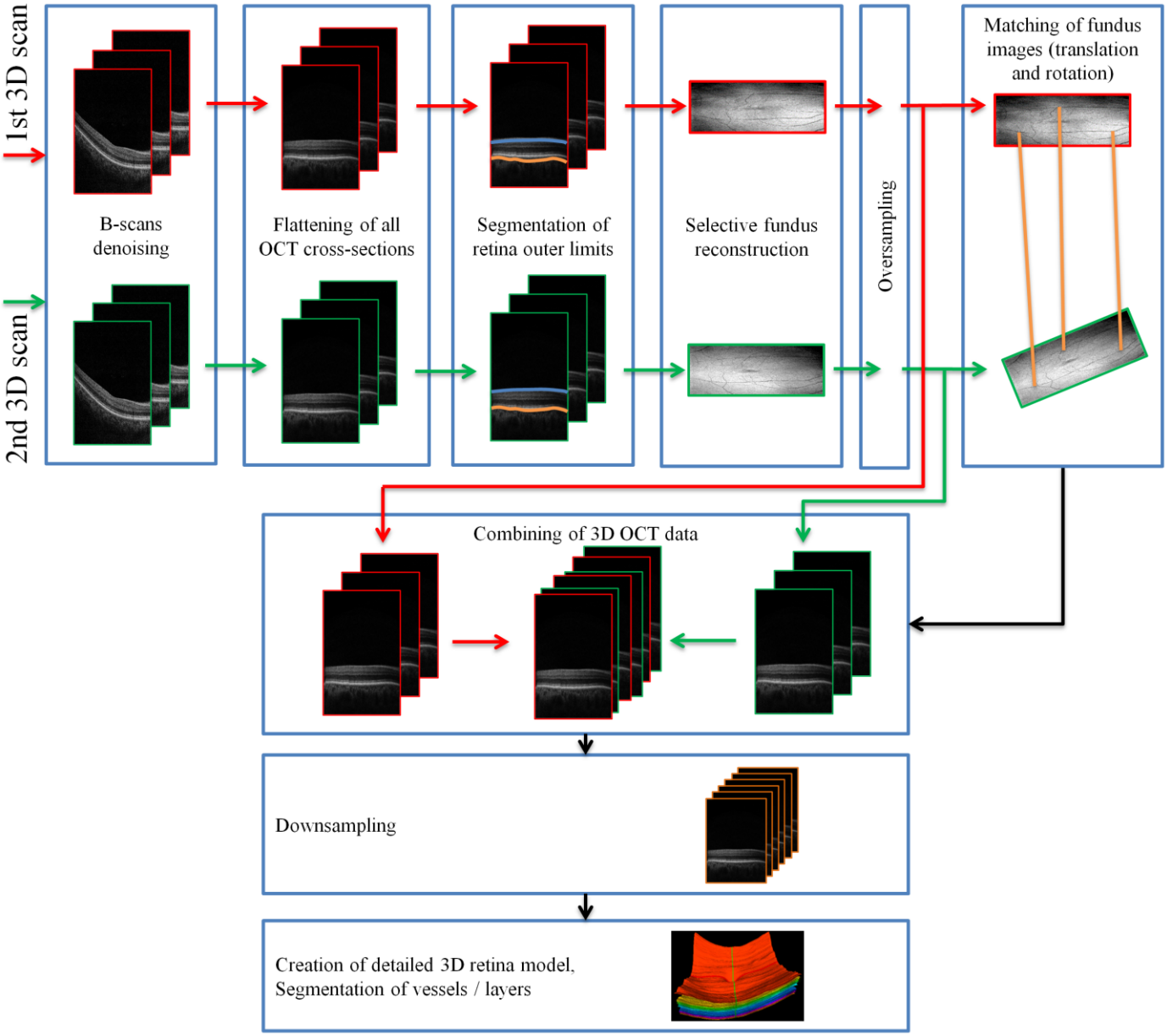

Figure 2. General scheme of the proposed algorithm

2) B-scans flattening

As a preparation procedure for retina layers segmentation, that discourages strong curvature or irregularities, we perform image flattening.

This operation is based on an estimate of the most hyper-reflective retina layer, namely retinal pigment epithelium (RPE). In each column the brightest pixel is located to form a curve representing the retina shape. From this contour we remove outliers, defined as points standing out more than 25 pixels from the mean in each height of the image (in the horizontal direction). Next, the left points are fit with a second order polynomial. Based on this estimate each column is shifted up or down, generating an image in which RPE points present a flat line. This procedure is repeated for each cross-section, so that the RPE layer forms a continuous plane throughout the whole 3D scan. Additionally, every 3D scan is flattened to the same height, thus eliminating the need for data matching in the third direction (depth of the scan).

3) Segmentation of outer retina layers

For the purpose of generating the selective fundus reconstruction, we perform segmentation of outer retina layers: inner limiting membrane (ILM – top layer) and RPE (bottom layer). The layers segmentation is performed independently in each B-scan based on the graph analysis technique introduced in [26] and extended for pathological eyes in [27].

4) Selective fundus reconstruction

The volumetric data between the segmented retina layers represents the topography of retina including its vessels. A projection of pixel values in the outlined region illustrates an image of retina as seen through the OCT lens, normally called the fundus image. Such a fundus image is suitable for preliminary matching the data in 2D. It should be mentioned that reconstruction of the fundus from the segmented volume reduces the influence of noise present in the rest of the scan.

5) Data oversampling

To achieve a sub-pixel accuracy in the matching step, the data is first oversampled. The selected scale factor determines the precision with which the reconstructed fundus images will be aligned. For this study we selected a scale factor of 4 with bicubic interpolation.

6) Matching of fundus images

Each fundus image reconstructed from 3D scans can be treated as a view of the same scene (view of the retina). During this step the translation and rotation between the oversampled input images is calculated to ascertain the motion estimation. The detailed description of this step is given in section II C.

7) Combining of 3D OCT data

Next, based on the calculated motion estimation the volumetric data is combined into a single high resolution 3D scan. Since the tissue is already aligned to a specific depth of the scan, the combining is performed on each B-scan row independently.

Various methods can be selected for this procedure. We investigated three variations of an algorithm relying on *k*-nearest geometric neighbors (k-NN). Section II D details the proposed solutions.

8) Data downsampling

After achieving the super-resolution scan, the data is down sampled. For proper ratio between vertical and horizontal directions of the scan, the target scan has the original width. The target height, however, has the same value as the width, thus, creating a square projection of the square tissue area. This means that the information in the horizontal direction is preserved, while the data in the vertical direction is enhanced.

9) Creation of model / Tissue segmentation

The data samples obtained with the use of this algorithm can be further analyzed for detailed layers and vessels segmentation as well as pathology detection.

Figure 2 illustrates the described algorithm on two 3-D OCT scans.

C. Registration step (Matching of images)

Let us consider the SR image I_S as pixels aligned on an evenly spaced grid, and a set of N LR observations $I_1, I_2, \dots I_N$ as a coarse representation of this image. We can define a relation between them, to be a result of the perspective transformation M_n with a downsampling parameter D_n in the following manner:

$$\forall n \in \langle 1, N \rangle : I_n = \mathrm{D}_n M_n I_S \qquad (1)$$

The scaling parameter D_n in the examined example has a fixed value of 1 in the horizontal direction and 2.73 in the vertical direction. In other words, a magnification of 2.73 of pixels in the vertical direction would create a square image with respect to the examined tissue area.

Through performing the motion estimation procedure on a set of LR observations we can derive the locations of each pixel from I_n image on the HR grid. This registration procedure allows us to align the I_n observations with respect to the I_S target image. The matching operation can be executed both in the spatial and frequency domain. For this step of the algorithm we utilized an implementation created by Robinson Laundon, based on the Fourier-Mellin transform [28], although other algorithms as SIFT or SURT are also appropriate.

D. Reconstruction step (Combining of images)

As was reported before, there are many possible algorithms for performing the reconstruction step, of which the majority is based on some variation of the nearest neighbor interpolation. Following this course of intuitive approach, we investigated the feasibility of utilizing three most promising k-NN methods for our purpose [29]. The principle of k-NN approach with $k = 1$ is illustrated in Fig. 3 on the example of two input images.

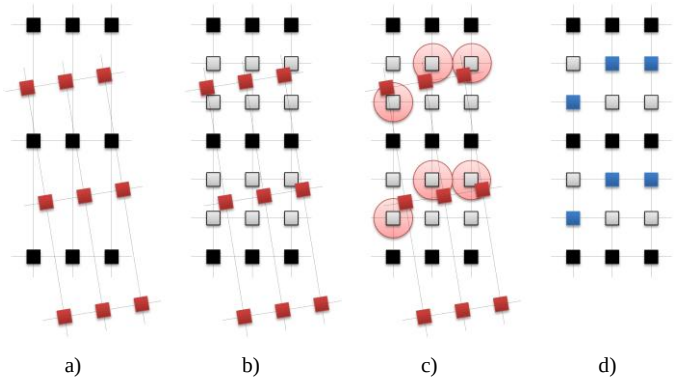

a) b) c) d)

Figure 3. Maximizing informative content

In this scheme, the black squares represent pixels from image I_1 and red squares − pixels from image I_2. Both sets of pixels are already aligned after the registration step (Fig. 3a).

In the next step we create a dense grid of pixels for the target HR picture (illustrated by both black and gray squares – Fig. 3b). Black squares represent the pixels that correspond to the pixels from I_1, while gray squares illustrate newly inserted pixels. It should be noted that the new pixels are added only in the horizontal direction, as that is the direction, the detailed representation is searched for.

Fig. 3c illustrates the nearest neighbors selected for each matched pixel. The final image I_S is composed of pixels from both images, as is shown in Fig. 3d.

We investigated three variants of the algorithm. In each of them the pixels used for calculating the new HR pixels are chosen differently. For the investigated approaches we are considering a single pixel in the HR grid p and its nearest pixel from each LR image I_n as p_n, with n ranging from 1 to N – the number of scans used for reconstruction. The position of each p_n pixel with respect to the HR grid is calculated from the matrixes M_n obtained during the registration procedure.

The details of the selected methods are described in the following subsections and illustrated in Fig. 4.

1) 1-NN method

The simplest, fastest and crudest variation uses only 1 input pixel ($k = 1$), as is shown in Fig. 4a. The value of the closest neighboring pixel (illustrated with red square) among all possible p_n pixels (black squares) is selected to be copied into the target image (blue square).

2) 3-NN method

Fig. 4b demonstrates the idea of selecting 3 of the nearest pixels to contribute to the final value of p ($k = 3$). The resulting pixel is calculated as a weighted average of the chosen three closest ones. The weights w_i for the averaging

process are defined as normalized values of inverse proportion of the distances between the selected pixels $p_i, i \in \langle 1, k \rangle$ and the target pixel p:

$$p = \frac{1}{k}\sum_{i=1}^{k} w_i p_i \quad (2)$$

$$w_1 + w_2 + \cdots + w_k = 1 \quad (3)$$

3) R-NN method

The last method finds all pixels p_n from contributing scans, that fall into the circular region formulated from a beforehand chosen radius R. Point p is set as the center of the delineated circle, as illustrates Fig. 4c. In this case the final pixel value is also calculated as the weighted average of the found pixels, with the use of equations (2) and (3). The k parameter in this method variant can be different for each pixel and is dependent on the p_n pixels that are found within the circular region.

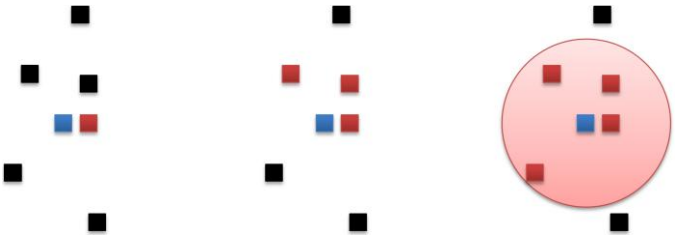

a) b) c)

Figure 4. Variations of k-NN

III. EXPERIMENTS

A. Dataset

The proposed algorithms were tested on a set of three-dimensional cross-sections of macula acquired with the use of the Avanti RTvue device. The database consists of 40 scans gathered from 5 patients, for whom both eyes were examined 4 times.

The obtained samples included both healthy and diseased retinas: two of the eyes were classified with idiopathic macular hole (IMH), one with vitreomacular adhesion (VMA), two with vitreomacular traction (VMT) and epiretinal membrane (ERM), five eyes came from healthy volunteers.

The registration and reconstruction steps of the experiment were performed in the Matlab/Simulink environment. The workstation used for testing was a 64-bit PC with Windows OS, Intel i7 processor, and 8 GB RAM.

B. Results

1) Validation of the proposed solution

Standard quantitative validation approach for super-resolution algorithms is based on comparison of the generated SR image to a single HR image, either obtained with the increased resolution or being a source image for creating LR images. Such procedure is not feasible in this application, since it is not possible to acquire a 3D OCT image with increased resolution. In such case we have to refer to the subjective quality assessment by visual inspection of B-scans and fundus images.

For that, we present examples of B-scans and fundus images obtained with the earlier described method variants using various numbers of scans. Fig. 5 illustrates a vertical slice from Fig. 1b after denoising, flattening, and resizing with the bicubic interpolation. Fig. 6-8 represent the same vertical slice obtained from combining 3 scans with 1-NN, 3-NN and R-NN method variants. Fig. 9 illustrates the equivalent of Fig. 1a after performing super-resolution with 3 scans and 3-NN method.

Comparing Fig. 5 with Fig. 6-8, it is clearly visible that the proposed solution improves quality of the resulting image. Noise present in the super-resolved images is reduced and intraretinal layers are more distinguishable. Additionally, Fig. 7 and 8 show even more smoothing of the tissue, but differences between them are imperceptible, suggesting that both methods are equally effective.

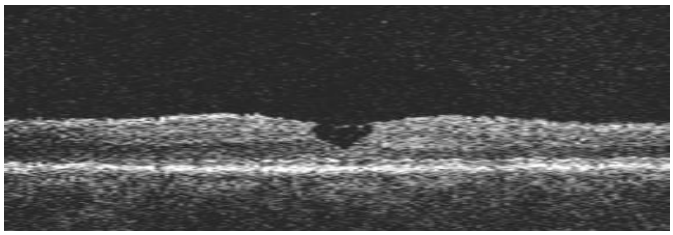

Figure 5. B-scan in vertical direction from a single 3D scan with bicubic interpolation

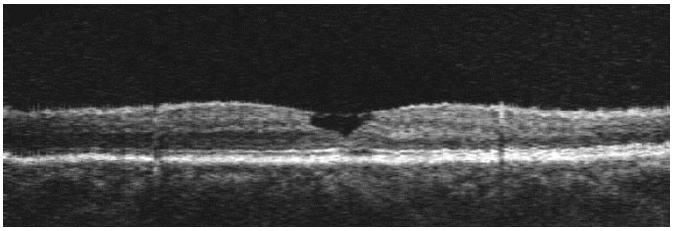

Figure 6. Reconstructed B-scan in vertical direction, obtained from 3 scans with 1-NN method

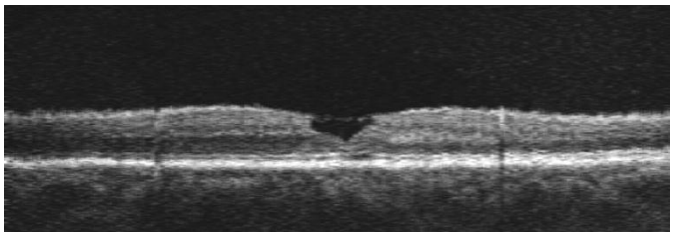

Figure 7. Reconstructed B-scan in vertical direction, obtained from 3 scans with 3-NN method

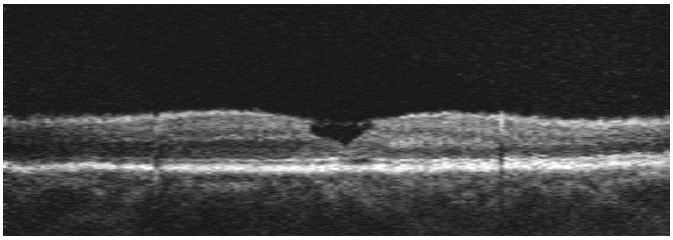

Figure 8. Reconstructed B-scan in vertical direction, obtained from 3 scans with R-NN method

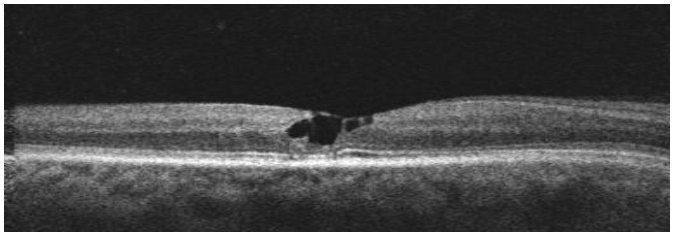

Figure 9. B-scan in horizontal direction obtained from 3 scans with 3-NN method

The original fundus images from 4 OCT scans obtained for one patient are presented in Fig. 10. As it can be seen, each scan demonstrates different illumination properties. Fig. 11 shows a combination of two of these scans with the use of various parameters. Fig. 12 illustrates influence of the number of input scans on quality of the super-resolved fundus image with 1-NN method.

Analyzing Fig. 11 we derived a conclusion that application of any of the proposed methods improves visibility of blood vessels especially in the upper section of fundus image with respect to any fundus image in Fig. 10. Furthermore, both 3-NN and R-NN methods present similar image quality.

It should be also noted that adaptation of the information from more than 2 scans improves the visibility and identification of vessels in fundus images, as can be seen in Fig. 12. Underexposed areas are enhanced and vessel tracks for small vessels are clearly visible. This might be useful for the application of vessels segmentation.

Time consumption analysis gives an average of 21 seconds for 1-NN method, 45 seconds for R-NN method and 81 seconds for 3-NN method. This suggests that a good quality SR OCT scan can be acquired with the use of only 1 nearest neighbor, while maintaining relatively low computational cost. Additionally, it might be sufficient to perform R-NN search, that gives similar result to the 3-NN method, but with less time consumption. The reason for that, is the number of candidates selected in the R-NN reconstruction step, which is in many cases lower than 3.

2) Selection of parameters

Another important feature of the algorithm is the selection of the number of input images. The authors of [29] postulated that for the super-resolution of a single image in both directions with scale m it is advisable to use at least m^2 LR frames.

Following this path of thinking for our application, were magnification is equal to m but in only one direction (the number of pixels in the second direction does not increase), we suggest that at least m LR frames should be used to obtain a good quality SR image. This can be confirmed by careful inspection of Fig. 12, in which significant differences can be seen between Fig. 12a, 12b, and 12c (each added scan provides new information and improves quality of the fundus image). In comparison, Fig. 12d does not introduce new valuable information in comparison to Fig. 12c.

The second parameter that needs to be selected is the radius R for the R-NN method variant. If the delineated circle includes more than one pixel from each LR image, a blurring effect might occur. To avoid this, we suggest that the R value was slightly less than the distance between pixels in a single LR image in the vertical direction.

3) Noise reduction

Additional advantage of the proposed algorithm is noise reduction. Nearly every report on SR assumes that the noise present in LR observations is a white Gaussian noise, with equal variance in all LR images [7]. The noise present in the OCT images is a speckle type noise, and an averaging technique utilizing several scans (as 3-NN and R-NN method variants) was proven to be successful for reducing this type of noise. This is also confirmed by Fig. 9, which represents the same slice as Fig. 1a and is much less obscured by noise with visibly distinguishable tissue areas.

IV. CONCLUSIONS

The paper describes an idea of super-resolving the 3D OCT data for improved quality image analysis. The proposed solution to enhance retina images provides valuable information for detailed tissue segmentation or modeling.

Using a set of B-scan images, the algorithm performs matching and combining data based on the selectively reconstructed fundus images. The oversampling procedure assures sub-pixel accuracy, and the obtained SR scan is substantially less noisy.

Replacing the sensor in the OCT device may be very expensive. Thus the software-based super-resolution technique it is possible to obtain high resolution data in a fast and inexpensive way. One high-resolution scan is difficult to acquire for old and pathological eyes, as opposed to several small ones that take short time and can be acquired in a time period of several minutes.

The proposed research has a potential to significantly impact the clinicians' approach to analyze retinal pathologies. The purposefulness of the described approach was confirmed by a group of ophthalmology experts.

In the future work, we plan to conduct an experimental research aimed at enhancement of computational efficiency by implementing parallel computing techniques.

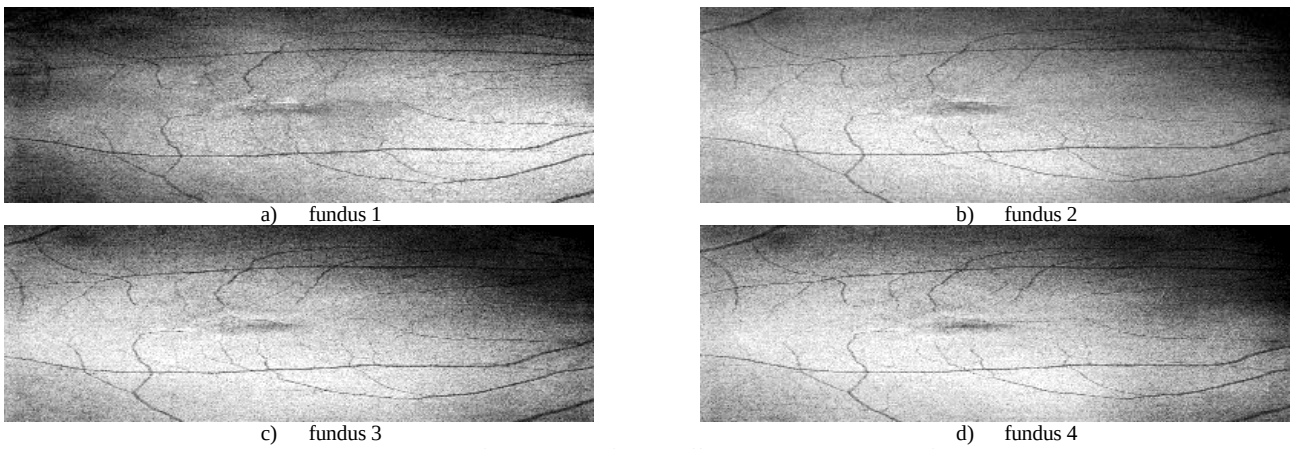

a) fundus 1 b) fundus 2

c) fundus 3 d) fundus 4

Figure 10. Reconstructed fundus images from 4 different OCT examinations of one patient

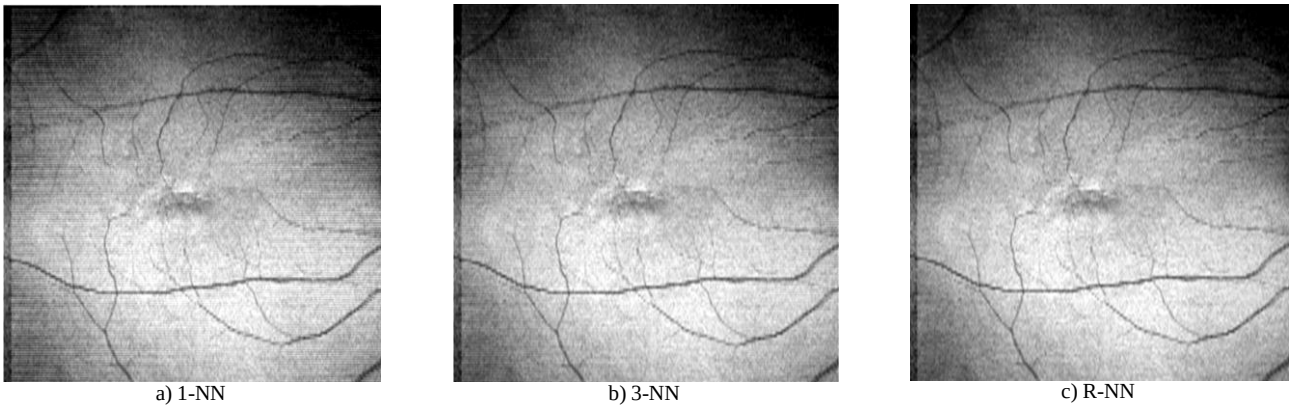

a) 1-NN b) 3-NN c) R-NN

Figure 11. Resulting super-resolved fundus images obtained from 2 scans with 3 variants of reconstruction method

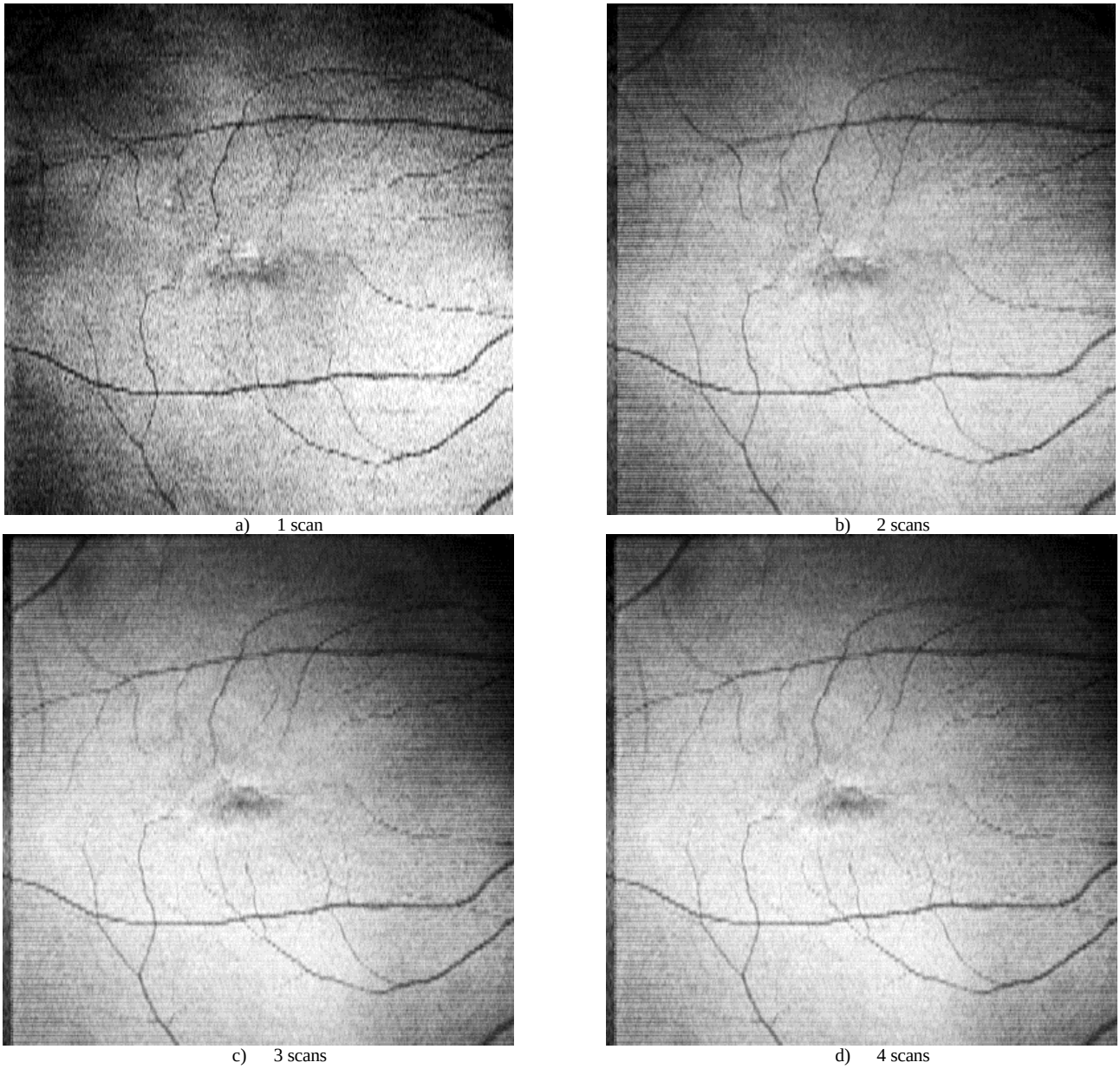

a) 1 scan b) 2 scans

c) 3 scans d) 4 scans

Figure 12. Resulting super-resolved fundus images composed of various number of input scans and 1-NN reconstruction method

REFERENCES

[1] M. Codenotti, L. Iuliano, G. Fogliato, and et al., "A novel spectral-domain optical coherence tomography model to estimate changes in vitreomacular traction syndrome," *Graefes Arch Clin Exp Ophthalmol*, 2014.

[2] P. Stalmans, J. S. Duker, P. K. Kaiser, J. S. Heier, P. U. Dugel, A. Gandorfer, J. Sebag, and J. A. Haller, "OCT-based interpretation of the vitreomacular interface and indications for pharmacologic vitreolysis," *Retina*, vol. 33, no. 10, pp. 2003–2011, 2013.

[3] R. Bernardes, T. Santos, and J. Cunha-Vaz, "Increased-Resolution OCT Thickness Mapping of the Human Macula: A Statistically Based Registration," *Investigative Ophthalmology & Visual Science*, vol. 49, no. 5, pp. 2046–2052, May 2008.

[4] I. Topcon Medical Systems, *Swept Source OCT with Multimodal True Fundus Imaging. Topcon Triton DRI OCT Model Datasheet*. 2014.

[5] Optovue and Inc., *RTVue XR 100 Avanti Edition. User manual*. 2014.

[6] Optopol, *SOCT Copernicus HR. User Manual Software Version 4.3.0*. 2011.

[7] J. Simpkins and R. L. Stevenson, "Mathematical Optics: Classical, Quantum, and Computational Methods," CRC Press, 2012, pp. 555–578.

[8] A. Lapini, F. Argenti, A. Piva, and L. Bencini, "Comparison of Super-Resolution Methods for Quality Enhancement of Digital Biomedical Images," in *2014 8th International Symposium on Medical Information and Communication Technology (ISMICT)*, 2014, pp. 1–5.

[9] R. R. Jillela and A. Ross, "Adaptive Frame Selection for Improved Face Recognition in Low-Resolution Videos," in *Proceedings of International Joint Conference on Neural Networks*, 2009, pp. 1439–1445.

[10] G. Fahmy, "Super-Resolution Construction of IRIS Images from a Visual Low Resolution Face Video," in *24 th NATIONAL RADIO SCIENCE CONFERENCE (NRSC 2007)*, 2007, no. C27, pp. 1–6.

[11] M. Shimizu, H. Kariya, T. Goto, S. Hirano, and M. Sakurai, "Super-Resolution for X-ray Images," in *IEEE 4th Global Conference on Consumer Electronics (GCCE)*, 2015, pp. 246–247.

[12] W. E. Hakimi and S. Wesarg, "Accurate Super-Resolution Reconstruction for CT and MR Images," in *Proceedings of the 26th IEEE International Symposium on Computer-Based Medical Systems*, 2013, pp. 445–448.

[13] Y. Kondo, X.-H. Han, and Y.-W. Chen, "Two-Step Learning Based Super Resolution and Its Application to 3D Medical Volumes," in *2015 IEEE 4th Global Conference on Consumer Electronics (GCCE)*, 2015, pp. 326–327.

[14] E.-U. Lin, M. McLaughlin, and A. A. Alshehri, "Medical Image Segmentation using Multi-Scale and Super-Resolution Method," in *2014 IEEE Applied Imagery Pattern Recognition Workshop (AIPR)*, 2014, pp. 1–5.

[15] M. Jobia, R. Gifty, K. Dayanandhan, and J. S. Sony, "PET Image Super Resolution Using a Novel Algorithm in Low Resolution Sinogram Reconstruction," in *2013 International Conference on Circuits, Power and Computing Technologies (ICCPCT-2013)*, 2013, pp. 904–907.

[16] N. Zhao, Q. Wei, A. Basarab, D. Kouam´e, and J.-Y. 1 Tourneret, "Single image super-resolution of medical ultrasound images using a fast algorithm," in *2016 IEEE 13th International Symposium on Biomedical Imaging (ISBI)*, 2016, pp. 473–476.

[17] A. Vahadane, N. Kumar, and A. Sethi, "Learning based super-resolution of histological images," in *2016 IEEE 13th International Symposium on Biomedical Imaging (ISBI)*, 2016, pp. 816–819.

[18] L. G. Villanueva, G. M. Callicó, F. Tobajas, S. López, V. D. Armas, J. F. López, and R. Sarmiento, "Medical Diagnosis Improvement through Image Quality Enhancement Based on Super-Resolution," in *2010 13th Euromicro Conference on Digital System Design: Architectures, Methods and Tools*, 2010, pp. 259–262.

[19] J. S. Isaac and R. Kulkarni, "Super Resolution Techniques for Medical Image Processing," in *2015 International Conference on Technologies for Sustainable Development (ICTSD-2015)*, 2015, pp. 1–6.

[20] Y. Iwamoto, X.-H. Han, S. Sasatani, K. Taniguchi, and Y.-W. Chen, "Super-Resolution of Medical Volumes Based on Principal Component Regression," in *2011 6th International Conference on Computer Sciences and Convergence Information Technology (ICCIT)*, 2011, pp. 945–948.

[21] D.-H. Trinh, M. Luong, F. Dibos, J.-M. Rocchisani, C.-D. Pham, and T. Q. Nguyen, "Novel Example-Based Method for Super-Resolution and Denoising of Medical Images," *IEEE TRANSACTIONS ON IMAGE PROCESSING*, vol. 23, no. 4, pp. 1882–1895, 2014.

[22] Y.-H. Wang, J.-B. Li, and P. Fu, "Medical Image Super-resolution Analysis with Sparse Representation," in *2012 Eighth International Conference on Intelligent Information Hiding and Multimedia Signal Processing*, 2012, pp. 106–109.

[23] M. F. Kraus, B. Potsaid, M. A. Mayer, R. Bock, B. Baumann, J. J. Liu, J. Hornegger, and J. G. Fujimoto, "Motion correction in optical coherence tomography volumes on a per A-scan basis using orthogonal scan patterns," *Biomedical Optics Express*, vol. 3, no. 6, pp. 1182–1199, Jun. 2012.

[24] M. Szkulmowski and M. Wojtkowski, "Averaging techniques for OCT imaging," *Optics Express*, vol. 21, no. 8, pp. 9757–9773, 2013.

[25] A. Stankiewicz, T. Marciniak, A. Dąbrowski, M. Stopa, P. Rakowicz, and E. Marciniak, "Metody poprawy dokładności automatycznej segmentacji obrazów w interfejsach biometrycznych OCT," in *XV Krajowa Konferencja Elektroniki, XI Interfejsy człowiek-komputer*, 2016, pp. 345–353.

[26] S. J. Chiu, X. T. Li, P. Nicholas, C. A. Toth, J. A. Izatt, and S. Farsiu, "Automatic segmentation of seven retinal layers in SDOCT images congruent with expert manual segmentation," *Optics express*, vol. 18, no. 18, pp. 19413–19428, 2010.

[27] A. Stankiewicz, T. Marciniak, A. Dąbrowski, P. M. Rakowicz Stopa, and E. Marciniak, "Improving segmentation of 3D retina layers based on graph theory approach for low quality OCT images," *Metrology and Measurement Systems*, vol. 23, no. 2, pp. 269–280, 2015.

[28] X. Guo, Z. Xu, Y. Lu, and Y. Pang, "An Application of Fourier-Mellin Transform in Image Registration," in *The Fifth International Conference on Computer and Information Technology (CIT'05)*, 2005, pp. 619–623.

[29] H. J. Seibel, S. Goldenstein, and A. Rocha, "Fast and Effective Geometric K-Nearest Neighbors Multi-Frame Super-Resolution," in *2015 28th SIBGRAPI Conference on Graphics, Patterns and Images*, 2015, pp. 103–110.